Broadband Noise Prediction of Two Small Hovering Rotors using FUN3D-ANOPP2

Christopher S. Thurman*, Li Wang[†], Emmett M. Padway[‡] NASA Langley Research Center, Hampton, VA, 23681

A computational study was performed on two small hovering rotors, the ideally twisted rotor and the optimum hovering 2-bladed rotor, using FUN3D-ANOPP2. The effects of different inviscid upwinding techniques and temporal resolutions on aerodynamic performance and acoustic prediction were compared against experimental data obtained in the Small Hover Anechoic Chamber facility at the NASA Langley Research Center. Decreasing the numerical dissipation with κ tuning or by using a higher-order inviscid flux reconstruction scheme was shown to improve aerodynamic performance predictions when compared to measured data for most cases. The effect of dissipation on the vorticity field was also seen to influence the amount of turbulence surrounding the vortex core of the first blade-vortex interaction (BVI), the coherence of the second and higher BVI vortex cores, and the downstream breakdown of the rotor wake for both rotor geometries. Tonal and broadband noise predictions from simulation cases with lower dissipation were seen to agree better with the experiment for the ideally twisted rotor, whereas temporal resolution differences had negligible impact on the broadband noise results. Similar fundamental BPF directivity patterns were obtained by all simulation cases for the optimum hovering 2-bladed rotor, while the most accurate 2*BPF directivity trend, compared to the experiment, was predicted by the lower-dissipation case at the coarse temporal resolution, albeit with an amplitude underprediction. Broadband noise spectral roll-off behavior was seen to occur at a higher frequency when using a finer temporal resolution for the optimum hovering 2-bladed rotor, unlike for the ideally twisted rotor geometry. The broadband noise prediction for the optimum hovering 2-bladed rotor from the higher-dissipation case at the coarse temporal resolution was also seen to predict a tone centered around approximately 8.5 kHz, which was similar in amplitude to the measured tone around 16.5 kHz.

Nomenclature

c = rotor blade chord length, m G_{xx} = power spectral density, Pa²/Hz M_{tip} = Mach number at the rotor blade tip

 N_b = number of rotor blades p_{ref} = reference pressure, 20 μ Pa

 \bar{p}_{rms} = root mean square of the acoustic pressure, Pa

R = rotor radius, m

 Re_{tip} = Reynolds number at the rotor blade tip

SPL = sound pressure level, dB

v = vector of local velocity components, m/s

y = radial observer location relative to the center of rotor rotation, m

 y^+ = normalized wall distance

 Δf = narrowband spectra frequency resolution, Hz

 $\Delta \psi$ = flow solver time step, deg

 Δc = grid spacing in the chordwise direction Δr = grid spacing in the spanwise direction

^{*}Research Aerospace Engineer, Aeroacoustics Branch, AIAA Member; christopher.thurman@nasa.gov

[†]Research Aerospace Engineer, Computational Aerosciences Branch, AIAA Associate Fellow; li.wang@nasa.gov

^{*}Research Aerospace Engineer, Aeroelasticity Branch, AIAA Member; emmett.m.padway@nasa.gov

 Δs = average grid spacing in wake resolution region Θ_{obs} = observer angle relative to rotor plane, deg

 θ_{tw} = rotor blade twist, deg

 θ, θ_3 = CFSR dissipation tuning parameter κ, κ_3 = UMUSCL dissipation tuning parameter

 ρ = local density, kg/m³ Ω = rotor speed, RPM ω = vorticity, 1/s

I. Introduction

Recent years have seen considerable interest in advanced air mobility (AAM) vehicles, capable of transporting personnel and packages across various environments in a safe and sustainable way. These vehicles are typically comprised of multirotor systems and generally range in size from small unmanned aerial systems (sUAS) to single- or multi-passenger vehicles designed for operation in urban environments. Though the AAM industry is growing at a rapid pace, noise is still a concern for the development and real-world application of these AAM vehicles. Designing AAM vehicles to minimize the acoustic impact on communities has motivated research in identifying and characterizing noise sources produced by sUAS vehicles, such as quadcopters. The study of these smaller sUAS vehicles or their isolated components (i.e., rotors) can aid the design of AAM vehicles with reduced acoustic emissions, mission planning, and trajectory optimization. With the intent to gain a better understanding of the larger AAM vehicles, this paper will computationally compare smaller sUAS rotors to experimentally available data.

The large differences in AAM vehicle size and operating conditions as opposed to traditional rotorcraft have led to a paradigm shift in the relative importance of different noise-generating mechanisms. For example, it has been shown that the stochastic, or broadband, portion of the noise emanating from sUAS vehicles lies in the most perceptible range of human audibility and may be a dominant noise source when compared to the deterministic, or tonal, noise components [1, 2]. This is in contrast to traditional rotorcraft, where tonal noise dominates over broadband noise. It is for this reason that, to date, limited work has been done toward development of prediction and analysis tools for rotor broadband noise.

Many tools exist for predicting both tonal and broadband noise [1, 3–5]. Modeling tonal noise typically requires an aerodynamic calculation to compute blade aerodynamic forces and kinematics and an acoustic propagation calculation to predict the noise at an observer location. For the aerodynamic calculation, a wide range of tools with varying fidelity exists: panel methods, blade element momentum theory (BEMT), comprehensive analysis codes (e.g., CAMRAD II, CHARM, and RCAS), traditional Reynolds-averaged Navier-Stokes (RANS) solvers (e.g., OVERFLOW2 and FUN3D), and higher-fidelity scale-resolving flow simulations (e.g., large eddy simulation and direct numerical simulation). Each of these tools is used to predict unsteady aerodynamic forces, which are in turn used to predict acoustic pressure at an observer location using an implementation of the Ffowcs Williams and Hawkings (FW-H) [6] equation. Similar approaches have been used to predict broadband noise directly from unsteady aerodynamic forces using the lattice-Boltzmann method [3, 4, 7–9], implicit large eddy simulation (LES) [10, 11], and hybrid RANS/LES [12–15].

To date, there is much ambiguity surrounding the prediction of rotor broadband noise using finite-volume Navier-Stokes solvers. Hybrid RANS/LES paradigms are the workhorse finite-volume method implemented for practical engineering problems; however, the boundary layer is often assumed to be fully turbulent and is modeled using RANS-based turbulence models. This assumption is counterintuitive to the prediction of broadband self-noise sources such as turbulent boundary layer trailing edge (TBLTE) noise since the noise-producing energetic turbulent structures in the outer region of the boundary layer are being modeled rather than resolved. This limitation is not unique to hybrid RANS/LES paradigms and was shown to also be problematic when using wall-functions unless some triggering mechanism (e.g., boundary layer trip) was used to produce turbulent structures in the boundary layer [7, 8, 16]. However, it may be argued that when external turbulence (i.e., within LES-resolving region of the grid) is present, such as blade wake entrained by tip vortices (i.e., blade-wake interaction (BWI) noise), accurate broadband noise predictions can be attained. Furthermore, it was shown in Refs. [12, 13] that hybrid RANS/LES employed by Navier-Stokes solvers is capable of predicting broadband noise sources such as BWI noise, blade-wake back-scatter noise, bluntness vortex shedding noise, and tip vortex formation noise, which were shown to be dominant noise sources for a small hovering ideally twisted rotor (ITR) geometry at its designed operating condition of $\Omega = 5500$ RPM [17]. There is still a lack of experience in predicting rotor broadband noise using unstructured finite-volume Navier-Stokes solvers, which generally have lower-order inviscid spatial discretization and more dissipation when compared to higher-order, structured Navier-Stokes codes.

The purpose of this work is to predict broadband noise using the unstructured-grid, node-based finite-volume Navier-Stokes solver, FUN3D, as the computational fluid dynamics (CFD) solver for two sUAS rotors: the ITR [3, 17] and the optimum hovering two-bladed rotor (OPT2) [7, 16]. A hybrid RANS/LES approach is utilized and the effects of using different inviscid upwinding techniques and different temporal resolutions are evaluated on both rotor geometries. Aerodynamic and acoustic predictions are compared to measured results from the Small Hover Anechoic Chamber (SHAC) facility at the NASA Langley Research Center.

II. Technical Approach

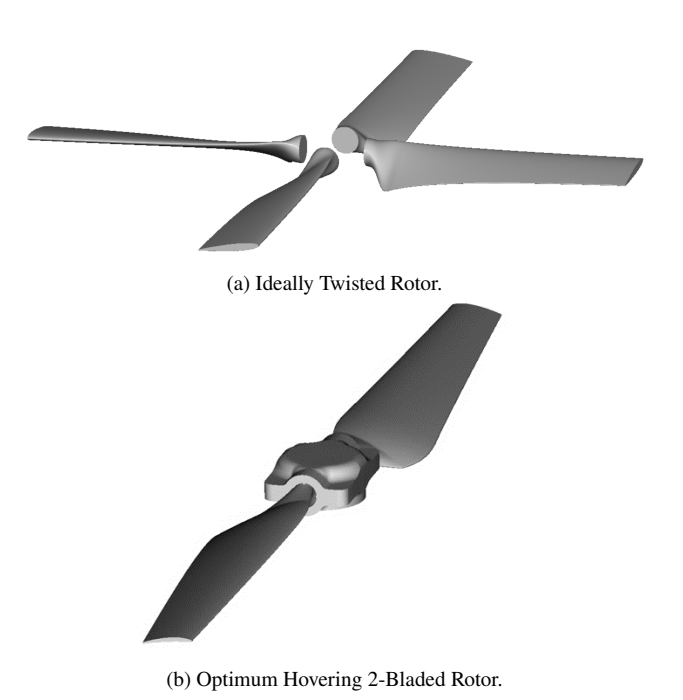
A. Rotor Designs

This work utilized two rotor geometries: the ITR and the OPT2, which are shown in Fig. 1. The ITR, shown in Fig. 1a, is a four-bladed ($N_b = 4$) rotor with a radius of R = 0.15875 m. This rotor uses an NACA 0012 airfoil profile along the blade span and has a constant chord length of c = 0.0254 m with a trailing edge thickness of 0.0157c. It was designed using BEMT to produce 11.12 N of thrust in hover at a rotor speed of $\Omega = 5500$ RPM ($M_{\rm tip} = 0.269$, $Re_{\rm tip} = 1.98 \times 10^5$). Further details of the ITR design can be found in Ref. [17].

The second rotor used in this work was the two-bladed $(N_b = 2)$ OPT2 shown in Fig. 1b. It should be noted that the hub shown in the figure was excluded from the simulations. The OPT2 has a radius of R = 0.1905 m, uses a cambered NACA 5408 airfoil profile along the blade span, and has a tip chord length of $c_{\text{tip}} = 0.01905$ m with a linear taper ratio of 2.25 to 1. The trailing edge thickness is equivalent to 3% of the chord length along the blade span (i.e., 0.03c(r)). The OPT2 was also designed using BEMT to produce 8.34 N of thrust in hover at a rotor speed of $\Omega = 3950$ RPM. ($M_{\rm tip} = 0.232$, $Re_{\rm tip} = 1.02 \times 10^5$). Further design details of the OPT2 can be found in Ref. [7]. The twist and chord distributions for both rotors are shown in Fig. 2 for clarity.

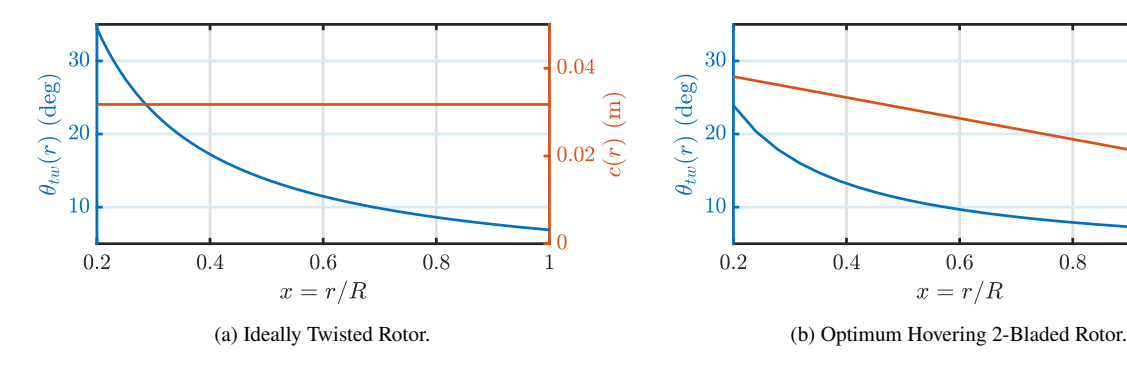
B. Computational Discretization

Since the simulations conducted in this work were for isolated hovering rotors, a rigid body rotation was applied to the entire computational domain using a rotating reference frame rather than utilizing overset grids. This methodology simplifies the grid generation process and reduces numerical error due to trilinear interpolation between rotating and stationary grids.



Rotor geometries.

0.8



Rotor twist and chord distributions.

A similar geometric discretization approach was utilized for both the ITR and OPT2 rotor blades, which consisted of surface grids containing 400 and 340 points in the spanwise direction and 249 and 255 chordwise points around the airfoil with 20 and 26 points around the blunt trailing edge, respectively. The average grid spacing in the spanwise direction for the ITR and OPT2 was $\Delta r_{\rm avg} = 0.012c_{\rm tip}$ and $\Delta r_{\rm avg} = 0.024c_{\rm tip}$, respectively, whereas the average grid spacing in the chordwise direction was $\Delta c_{\rm avg} = 0.009c_{\rm tip}$ for both rotors. A summary of the surface grid spacings is shown in Table 1 where the subscripts, LE, TE, and tip, denote grid clustering about the leading edge, trailing edge, and tip of the rotor blade.

Table 1 Rotor blade grid spacing summary.

Rotor	$\Delta r_{\rm avg}/c_{\rm tip}$	$\Delta r_{\rm tip}/c_{ m tip}$	$\Delta c_{\rm avg}/c_{\rm tip}$	$\Delta c_{ m LE}/c_{ m tip}$	$\Delta c_{\mathrm{TE}}/c_{\mathrm{tip}}$	No. TE Points
ITR	0.012	0.001	0.009	0.001	0.001	20
OPT2	0.024	0.002	0.009	0.002	0.002	26

An orthogonal advancing front algorithm was implemented within the commercial software package, Cadence[®] FidelityTM Pointwise[®], to orient the triangular surface elements such that two adjacent triangular elements, which share a hypotenuse, fit into a single orthogonal quadrilateral element. A visualization of the ITR surface grid is shown in Fig. 3 to highlight the spanwise grid clustering near the blade tip. Figure 3b shows the grid clustering used near the leading and trailing edges of the blade in the chordwise direction. It should be noted that care was taken to ensure minimal aspect ratio changes between the blade planform shown in Fig. 3a and the tip face region shown in Fig. 3b, which was accomplished by matching the grid clustering at their intersection.

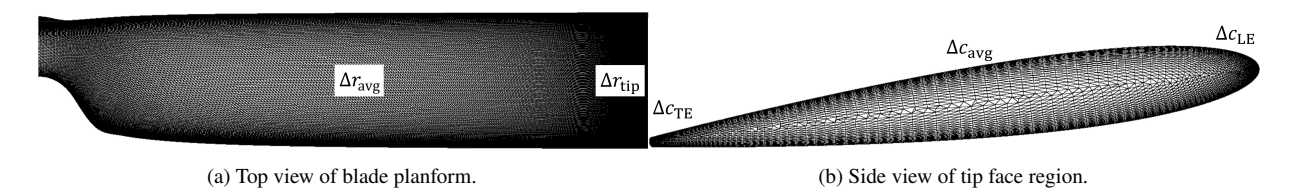


Fig. 3 Ideally twisted rotor surface grids.

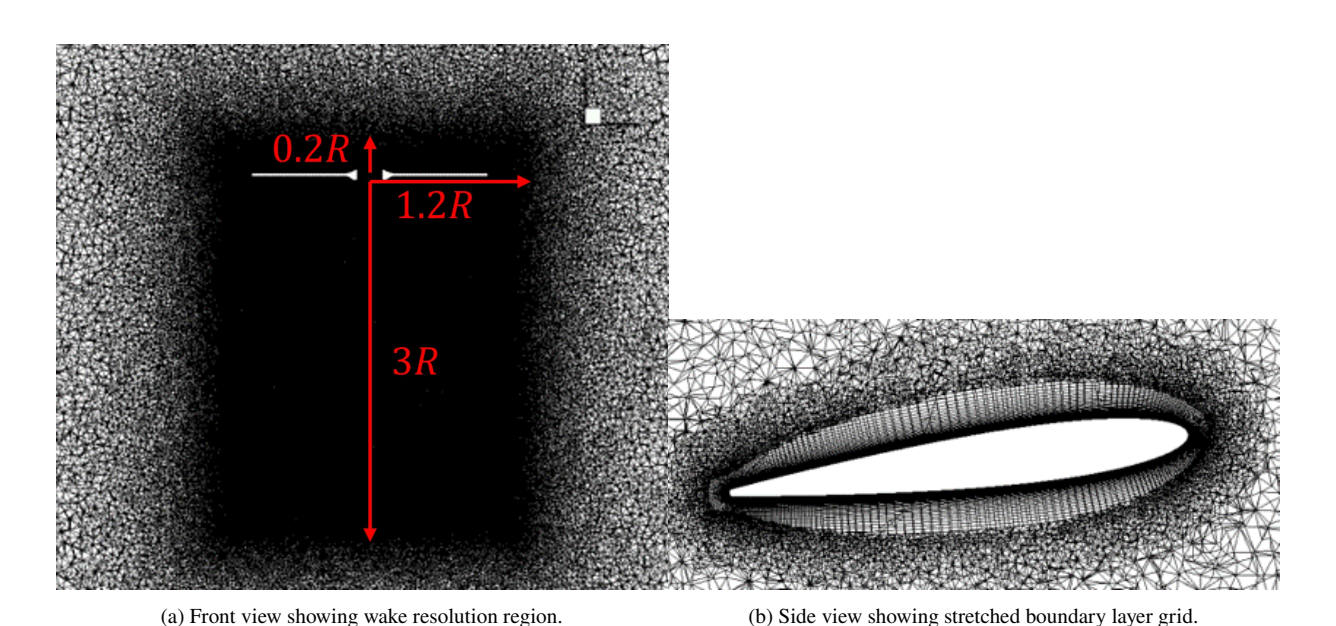


Fig. 4 Ideally twisted rotor volume grid.

The volumetric grid extended 50R away from the center of each rotor and consisted mostly of tetrahedron elements.

A wake resolution region, shown in Fig. 4a, extended approximately 3R below the center of each rotor and had an average cell spacing of $\Delta s = 0.05c_{\rm tip}$. Grid stretching was used to produce a boundary layer grid adjacent to the rotor geometry, shown in Fig. 4b for the ITR. The boundary layer grid for both rotors consisted of approximately 33 full layers and 69 total layers of volumetric prism elements with an initial wall-normal spacing such that $y^+ = 0.481$ and $y^+ = 0.405$ for the ITR and OPT2, respectively, based on the tip chord Reynolds number. A summary of the volumetric grids for both the ITR and OPT2 is shown in Table 2. The computational volume discretization techniques discussed in this section closely resemble those successfully applied in Ref. [12] corresponding to a structured-grid Navier-Stokes solver and best practices determined by Chaderjian [18] for isolated hovering rotor simulations.

Table 2 Volumetric grid summary.

Rotor	Tetrahedron Cells	Pyramid Cells	Prism Cells	Total Cells	Total Points
ITR	193,697,465	165,888	44,378,576	238,241,929	53,656,172
OPT2	706,012,571	52,812	21,610,140	727,675,523	124,832,339

C. Numerical Methods

FUN3D [19] is a node-centered, unstructured-grid, Navier-Stokes solver developed and maintained at the NASA Langley Research Center. FUN3D has a broad range of capabilities including steady and unsteady algorithms for solving the two- and three-dimensional Euler and RANS equations on static or dynamic mixed-element grid systems with the option for including overset grid topologies. FUN3D is widely used for a range of complex high-fidelity problems, including scale-resolving simulations [20–22], airframe noise applications [23, 24], and, more specific to this work, rotorcraft applications [25–28].

Conservation laws are discretized in FUN3D using a median-dual mesh approach where control volumes are built around each of the grid vertices and flux values are computed at the edge median of this 'dual mesh', which is bordered by the gray dashed line in Fig. 5. The inviscid flux values were calculated using Roe's flux-difference splitting scheme [29] in this work and can be written as:

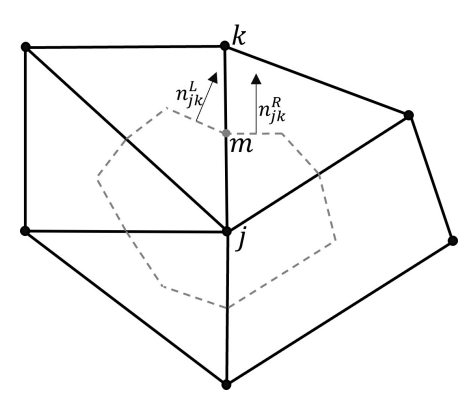


Fig. 5 Median-dual control volume around grid vertex.

$$\Phi_{jk} = \frac{1}{2} [\mathbf{f}_L + \mathbf{f}_R] - \frac{1}{2} \hat{\mathbf{D}}_n [\mathbf{u}(\mathbf{w}_R) - \mathbf{u}(\mathbf{w}_L)], \tag{1}$$

where $\mathbf{f} = \mathcal{F} \cdot \mathbf{n}_{jk}$ is the flux projected along the directed-area vector, which is the sum of all dual faces shared by the edge, $\mathbf{n}_{jk} = \hat{\mathbf{n}}_{jk} | \mathbf{n}_{jk}|$, $\hat{\mathbf{D}}_n = |\partial \mathbf{f}/\partial \mathbf{u}|$ is the dissipation matrix evaluated with the Roe averages of the reconstructed primitive variables at the left and right sides of the edge midpoint, \mathbf{w}_L and \mathbf{w}_R . In Eq. (1), \mathbf{u} is the vector of conserved variables. For the reconstructed primitive variables, $\mathbf{w} = (\rho, \mathbf{v}, p)$, FUN3D employs the second-order accurate unstructured monotonic upstream scheme for conservation laws (UMUSCL) scheme [30], which was later extended by Yang and Harris [31] to read:

$$\mathbf{w}_{L} = \kappa \frac{\mathbf{w}_{j} + \mathbf{w}_{k}}{2} + (1 - \kappa) \left[\mathbf{w}_{j} + \hat{\partial}_{j} \mathbf{w}_{j} \right] + \kappa_{3} \tilde{\partial}_{j}^{3} \mathbf{w}, \tag{2}$$

$$\mathbf{w}_{R} = \kappa \frac{\mathbf{w}_{k} + \mathbf{w}_{j}}{2} + (1 - \kappa) \left[\mathbf{w}_{k} + \hat{\partial}_{k} \mathbf{w}_{k} \right] + \kappa_{3} \tilde{\partial}_{k}^{3} \mathbf{w}, \tag{3}$$

where

$$\tilde{\partial}_{j}^{3}\mathbf{w} = \frac{1}{2} \left\{ \hat{\partial}_{j}\mathbf{w}_{k} - \hat{\partial}_{j}\mathbf{w}_{j} \right\} - \hat{\partial}_{j}^{2}\mathbf{w}_{j}, \quad \tilde{\partial}_{k}^{3}\mathbf{w} = \frac{1}{2} \left\{ \hat{\partial}_{k}\mathbf{w}_{j} - \hat{\partial}_{k}\mathbf{w}_{k} \right\} - \hat{\partial}_{k}^{2}\mathbf{w}_{k}, \tag{4}$$

and

$$\tilde{\partial}_j = (\mathbf{x}_m - \mathbf{x}_j) \cdot \nabla, \quad \tilde{\partial}_k = (\mathbf{x}_m - \mathbf{x}_k) \cdot \nabla.$$
 (5)

In Eqs. (2–5), \mathbf{x}_m denotes the position vector of the edge midpoint, and \mathbf{x}_j and \mathbf{x}_k denote the nodal position vectors of j and its neighbor, k. It should be noted that Eqs. (2) and (3) revert back to the UMUSCL scheme of Burg when

 $\kappa_3 = 0$. Typical FUN3D solution strategies for scale-resolving simulations entail the use of Burg's UMUSCL scheme (i.e., $\kappa_3 = 0$) with 'dissipation tuning' through the use of the variable κ in Eqs. (2) and (3). Commonly used values of this parameter are $\kappa = 0.5$ (i.e., blended between upwind and central differencing for mixed-type element grids) and $\kappa = 0.9$ (i.e., central differencing biased) [20, 22]. In these two cases, \mathbf{f}_L and \mathbf{f}_R in Eq. (1) are averaged between the left and right cells adjacent to the edge median using unweighted least-squares gradients.

Flux solution reconstructions have recently been investigated by Padway and Nishikawa [32], where it was shown that higher-order inviscid solutions are possible by flux reconstruction via chain rule differentiation:

$$\mathbf{f}_{L} = \theta \frac{\mathbf{f}_{j} + \mathbf{f}_{k}}{2} + (1 - \theta) \left[\mathbf{f}_{j} + \hat{\partial}_{j} \mathbf{f}_{j} \right] + \theta_{3} \tilde{\partial}_{j}^{3} \mathbf{f}, \tag{6}$$

$$\mathbf{f}_{R} = \theta \frac{\mathbf{f}_{k} + \mathbf{f}_{j}}{2} + (1 - \theta) \left[\mathbf{f}_{k} + \hat{\partial}_{k} \mathbf{f}_{k} \right] + \theta_{3} \tilde{\partial}_{k}^{3} \mathbf{f}, \tag{7}$$

where

$$\tilde{\partial}_{j}^{3}\mathbf{f} = \frac{1}{2} \left\{ \hat{\partial}_{j}\mathbf{f}_{k} - \hat{\partial}_{j}\mathbf{f}_{j} \right\} - \hat{\partial}_{j}^{2}\mathbf{f}_{j}, \quad \tilde{\partial}_{k}^{3}\mathbf{f} = \frac{1}{2} \left\{ \hat{\partial}_{k}\mathbf{f}_{j} - \hat{\partial}_{k}\mathbf{f}_{k} \right\} - \hat{\partial}_{k}^{2}\mathbf{f}_{k}, \tag{8}$$

$$\hat{\partial}_{j} \mathbf{f}_{j} = \left(\frac{\partial \mathbf{f}}{\partial \mathbf{w}}\right)_{i} \hat{\partial}_{j} \mathbf{w}_{j}, \quad \hat{\partial}_{k} \mathbf{f}_{k} = \left(\frac{\partial \mathbf{f}}{\partial \mathbf{w}}\right)_{k} \hat{\partial}_{k} \mathbf{w}_{k}, \tag{9}$$

$$\hat{\partial}_{j}^{2} \mathbf{f}_{j} = \hat{\partial}_{j} \left(\frac{\partial \mathbf{f}}{\partial \mathbf{w}} \right)_{j} + \left(\frac{\partial \mathbf{f}}{\partial \mathbf{w}} \right)_{j} \hat{\partial}_{j}^{2} \mathbf{w}_{j}, \quad \hat{\partial}_{k}^{2} \mathbf{f}_{k} = \hat{\partial}_{k} \left(\frac{\partial \mathbf{f}}{\partial \mathbf{w}} \right)_{k} + \left(\frac{\partial \mathbf{f}}{\partial \mathbf{w}} \right)_{k} \hat{\partial}_{k}^{2} \mathbf{w}_{k}. \tag{10}$$

This chain-rule-flux-solution reconstruction (CFSR) is third-order accurate [33] with $(\kappa, \kappa_3, \theta, \theta_3) = (arbitrary, 0, 1/3, 0)$ and fourth-order accurate with $(\kappa, \kappa_3, \theta, \theta_3) = (arbitrary, \kappa - 1, 1/3, 0)$, which are referred to as CFSR3 and CFSR4, respectively. Reference [32] showed that the CFSR schemes only provide higher-order accuracy on hexahedron cells and are second-order accurate with low dissipation and low error on other cell types.

To solve the unsteady RANS equations, a dual-time approach was utilized in this work where point-implicit multicolor Gauss-Siedel iterations were executed at each time step to sufficiently reduce the residuals of the linearized system of equations. An optimized second-order backward differencing scheme [34] (BDF2OPT) was used for the temporal integration with a physical time step correspondent to $\Delta\psi=0.25^\circ$ of azimuthal advancement, or 1440 steps per rotor revolution, for the coarse temporal resolution cases and $\Delta\psi=0.125^\circ$, or 2880 steps per rotor revolution, for the fine temporal resolution cases. For the mean flow viscous terms, the Green-Gauss theorem was used to compute cell-based gradients for a second-order approximation. A hybrid RANS/LES framework was used in this work for all simulations, where the Boussinesq assumption related the Reynolds stress in the RANS equations to a mean strain-rate tensor and turbulent eddy viscosity determined through turbulence model-based closures. Delayed detached eddy simulations (DDES) were used, which effectively switch between a RANS-based turbulence model in the boundary layer and a Smagorinsky-type LES elsewhere in the computational domain. The DDES method of Spalart et al. [35] was used in this study with the negative variant of the one-equation Spalart-Allmaras turbulence model and a rotation/curvature correction (DDES-neg-RC). Similar to the mean flow viscous terms, the Green-Gauss theorem was used to compute a second-order approximation to the turbulence model diffusion terms.

This work will investigate the effect of different inviscid flux calculations and different temporal resolutions on rotor aerodynamic performance and broadband noise prediction. The UMUSCL scheme of Burg [30] (i.e., $\kappa_3 = 0$) with $\kappa = 0.5$ and $\kappa = 0.9$, respectively, will first be evaluated at two different temporal resolutions (i.e., $\Delta \psi = 0.25^{\circ}$ and $\Delta \psi = 0.125^{\circ}$) on both the ITR and OPT2 geometries at their respective baseline hover operating conditions of $\Omega = 5500$ RPM and $\Omega = 3950$ RPM. The fourth-order CFSR (CFSR4) will then be evaluated on both rotor geometries. For the CFSR4 prediction, the parameters κ , κ_3 , θ , and θ_3 were set to $(\kappa, \kappa_3, \theta, \theta_3) = (1/2, -1/2, 1/3, 0)$. Another CFSR4 case, denoted as CFSR4- κ , where $(\kappa, \kappa_3, \theta, \theta_3) = (0.9, -0.1, 1/3, 0)$, was also evaluated on the ITR at $\Delta \psi = 0.25^{\circ}$ to determine the effects of dissipation tuning on the higher-order scheme. It should be noted again that the CFSR4 inviscid scheme is only fourth-order accurate on hexahedron elements but will produce low dissipation results with low error on the mixed-element grids in this work. Due to computational limitations, acoustic predictions were not performed for every simulated case. A summary of the predictions conducted in this work is shown in Table 3.

Table 3 Summary of prediction results.

Case	ITR Pr	edictions	OPT2 Predictions		
	$\Delta \psi = 0.25^{\circ} \Delta \psi = 0.125$		$\Delta\psi=0.25^{\circ}$	$\Delta\psi=0.125^\circ$	
$\kappa = 0.5$	All	All	All	Aero only	
$\kappa = 0.9$	All	All	All	All	
CFSR4	All	Aero only	Aero only	None	
CFSR4-κ	All	Aero only	None	None	

D. Acoustic Processing

Unsteady blade loading for simulations with acoustic predictions was sampled over approximately ten revolutions at a rate of 132 kHz or 264 kHz for the ITR and 94.8 kHz or 189.6 kHz for the OPT2 depending on the temporal resolution, once statistical convergence of aerodynamic forces and moments was established. These sampled data were then provided to the ANOPP2 [36] CFD Acoustic Propagation Tool (ACAPT) for the computation of propagated acoustic pressure time history (APTH) at observer locations using the impermeable Farassat's Formulation 1A (F1A) [37–39].

The calculated APTH from the ten revolutions of sampled data was separated into ten equally sized blocks corresponding to each revolution of rotor data. These ten revolutions of data were ensemble averaged to obtain a mean revolution of APTH, which is the periodic (i.e., tonal) acoustic component. This periodic acoustic component was then subtracted from the raw, aperiodic APTH from the ten revolutions of data, and the resultant residual APTH served as the stochastic (i.e., broadband) acoustic component. The following acoustic processing methods were then used and are similar to those used for the experimental data measured in the SHAC facility at the NASA Langley Research Center [17]:

1) The mean rotor revolution of predicted data was repeated enough times to attain a $\Delta f = 20$ Hz frequency resolution, which was then processed by treating the repeated rotor revolution data as an aperiodic signal, computing the fast Fourier transform (FFT) of the data with a Hanning window and no overlap, then using Eq. (11) to produce a narrowband spectrum of the predicted tonal noise sound pressure level (SPL);

$$SPL = 10\log_{10}\left(\frac{G_{xx} * \Delta f}{p_{ref}^2}\right),\tag{11}$$

where G_{xx} is the resultant power spectral density from the FFT calculation and $p_{ref} = 20 \mu Pa$.

2) For establishing tonal directivity patterns, the mean revolution of APTH was filtered using a second-order Butterworth narrow bandpass filter with a ± 20 Hz frequency band centered on the fundamental blade passage frequency (BPF) and first harmonic of the BPF (i.e., 2*BPF). This filter served the purpose of mitigating spectral leakage associated with different measurement and post-processing techniques. The root mean squared value of these filtered data, \bar{p}_{rms} , was used to calculate the amplitude of the BPFs on a logarithmic basis using:

$$SPL_{BPF} = 20\log_{10}\left(\frac{\bar{p}_{rms}}{p_{ref}}\right). \tag{12}$$

3) The extracted broadband noise signals from the computations were treated as aperiodic signals over which an FFT using a Hanning window with 50% overlap was also calculated using the ten revolutions of data. A block length of one revolution of residual APTH data was used, which resulted in a spectral resolution of $\Delta f = 91.68$ Hz. Equation (11) was then used without the Δf term to produce power spectral densities of the stochastic noise component.

III. Aerodynamic Results

This section presents aerodynamic simulation results for the ITR and OPT2 rotors computed with the unstructured-grid FUN3D solver using various flux reconstruction schemes and temporal resolutions. Residuals generally decreased by 4–5 orders of magnitude (OOM) for the mean flow equations and by 2–3 OOM for the turbulence model equation at each time step. The solution procedure began with freestream conditions, and initial flow transients were eliminated using a large time step (i.e., Δ =2.5°) over 10 rotor revolutions. Following this, simulations were conducted at the

desired time step with an additional 5 rotor revolutions to further eliminate flow transients. For simulation cases without acoustic results, one final rotor revolution was simulated for aerodynamic performance calculations. For simulation cases with acoustic results, unsteady surface pressure data were collected over approximately 10 rotor revolutions for subsequent acoustic analysis.

A. Ideally Twisted Rotor

In Table 4, the computed thrust and torque values averaged over one revolution for all ITR simulations are compared against experimental measurements reported in Ref. [17] from rotors fabricated using stereolithography. Reasonable agreement within approximately 11% of the experimental thrust and torque values can be seen for all ITR predictions with the $\kappa = 0.5$ case at $\Delta \psi = 0.125^{\circ}$ producing the best thrust prediction and the CFSR4- κ case at $\Delta \psi = 0.25^{\circ}$ yielding the best torque prediction.

Case	Experiment	$\Delta \psi = 0.25^{\circ}$				$\Delta \psi = 0.125^{\circ}$	
		$\kappa = 0.5$	$\kappa = 0.9$	CFSR4	CFSR4-κ	$\kappa = 0.5$	$\kappa = 0.9$
Thrust	10.1 N	9.24 N	9.20 N	9.26 N	9.27 N	9.29 N	9.09 N
Relative Diff.		8.51%	8.91%	8.32%	8.22%	8.02%	10.0%
Torque	-0.213 N-m	-0.191 N-m	-0.191 N-m	-0.192 N-m	-0.194 N-m	-0.191 N-m	-0.190 N-m
Relative Diff.		10.33%	10.33%	9.86%	8.92%	10.33%	10.80%

Table 4 ITR aerodynamic performance comparison.

It was shown in Ref. [12] that the dominant broadband noise sources for the ITR were caused by perpendicular blade-vortex interactions (BVIs). With that in mind, instantaneous vorticity visualizations on a vertical slice aligned with the quarter-chord location of a blade are shown in Fig. 6 for the simulated ITR cases at the coarse temporal resolution.

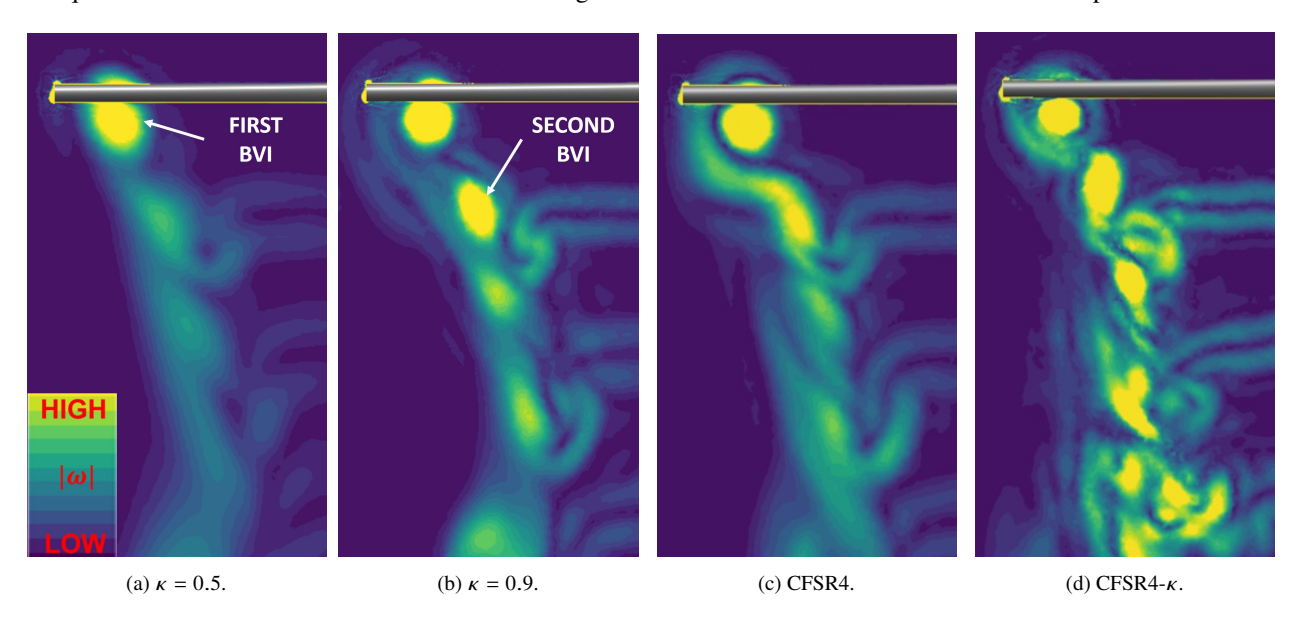


Fig. 6 ITR flow visualization of instantaneous vorticity magnitude along quarter-chord aligned vertical slice showing impingement of vortex from previous blade for $\Delta \psi = 0.25^{\circ}$ cases.

All four cases have similar vortex proximity to the rotor blade; however, the difference in dissipation has an effect on the turbulent field surrounding the vortex core of the first BVI, the coherence of the second and higher BVI vortex cores, and the downstream breakdown of the rotor wake. For example, Fig. 6a shows that the simulated case with the most numerical dissipation (i.e., $\kappa = 0.5$) predicted the least amount of turbulence around the vortex core and the least-coherent second and higher BVI vortices. Moreover, the effects of the increased dissipation on the rotor wake breakdown are apparent. Though the decreased dissipation in the $\kappa = 0.9$ case recovers some of the salient

features associated with the BVIs and has a very coherent second BVI vortex, this case does not lead to improved rotor performance predictions. Further investigation is needed to evaluate the source of the disparity in aerodynamic performance accuracy. It can also be seen in Fig. 6c that the CFSR4 case predicts the strongest and most-coherent structures around the main vortex core. Additional dissipation tuning in the CFSR4- κ case can be seen in Fig. 6d to reduce the size of the main vortex core and increase the size of the turbulent field surrounding the main core when compared to the CFSR4 case. It also appears that the CFSR4- κ case retains the BVI vortex structures further downstream and the wake breakdown appears to be caused by turbulent mixing rather than by dissipation as in the other three cases. It may not be possible to discern which of the four cases in Fig. 6 produces the most accurate vortex dynamics without experimental flow visualization techniques; however, by correlating these prediction visualizations to the aerodynamic performance comparison in Table 4, it may be inferred that the CFSR4- κ case is more accurate than the other three $\Delta \psi = 0.25^{\circ}$ cases.

B. Optimum Hovering 2-Bladed Rotor

In Table 5, the computed thrust and torque values averaged over one revolution for the OPT2 simulations are compared against experimental measurements reported in Ref. [16] from rotors fabricated using stereolithography.

Case	Experiment		$\Delta\psi=0.25^{\circ}$	$\Delta \psi = 0.125^{\circ}$		
Case		$\kappa = 0.5$	$\kappa = 0.9$	CFSR4	$\kappa = 0.5$	$\kappa = 0.9$
Thrust	8.67 N	7.42 N	7.58 N	7.83 N	7.11 N	7.65 N
Relative Diff.		14.42%	12.57%	9.69%	17.99%	11.76%
Torque	-0.159 N-m	-0.152 N-m	-0.153 N-m	-0.142 N-m	-0.147 N-m	-0.154 N-m
Relative Diff.		4.40%	3.77%	10.69%	7.55%	3.14%

Table 5 OPT2 aerodynamic performance comparison.



Fig. 7 Post-campaign visualization of OPT2 rotor blade [40].

The OPT2 predictions are shown to have a larger relative thrust difference to the measured data when compared to the torque difference for all cases except for the CFSR4 case, which may be explained by collective pitch and blade deflection uncertainties in the OPT2 experimental data [40]. A post-campaign visualization of an OPT2 rotor blade is shown in Fig. 7, which may allude to blade deflection during testing due to the structural rigidity of the stereolithography material (or lack thereof). The CFSR4 case at $\Delta \psi = 0.25^{\circ}$ in Table 5 can be seen to

produce the best thrust prediction when compared to the measured data, while the $\kappa = 0.9$ case at $\Delta \psi = 0.125^{\circ}$ shows the best torque agreement. In general, it can be said that decreasing the dissipation by increasing κ improves both thrust and torque predictions for the OPT2 geometry.

Visualizations of the OPT2 vorticity flow field are shown for the three $\Delta\psi=0.25^\circ$ cases in Fig. 8 with the same vorticity contour range as was used in the ITR visualization. Again, the finer temporal resolution results showed negligible differences in the vorticity field compared with the $\Delta\psi=0.25^\circ$ cases and are withheld. It can be seen in comparing Figs. 8a and 8b that the lower-dissipation case (i.e., $\kappa=0.9$) has three very coherent vortices followed by turbulent wake breakdown whereas the $\kappa=0.5$ case has only two distinct vortices followed by a much larger and less-coherent third vortex. Beyond this third vortex from the $\kappa=0.5$ case, the wake breakdown exhibits fewer fine-scale turbulent structures than the $\kappa=0.9$ case and appears to have some coherent structures within the wake breakdown. The CFSR4 case in Fig. 8c appears more similar to the $\kappa=0.5$ case than to the $\kappa=0.9$ case, in that it has two coherent vortices rather than three followed by wake breakdown with fewer turbulent structures.

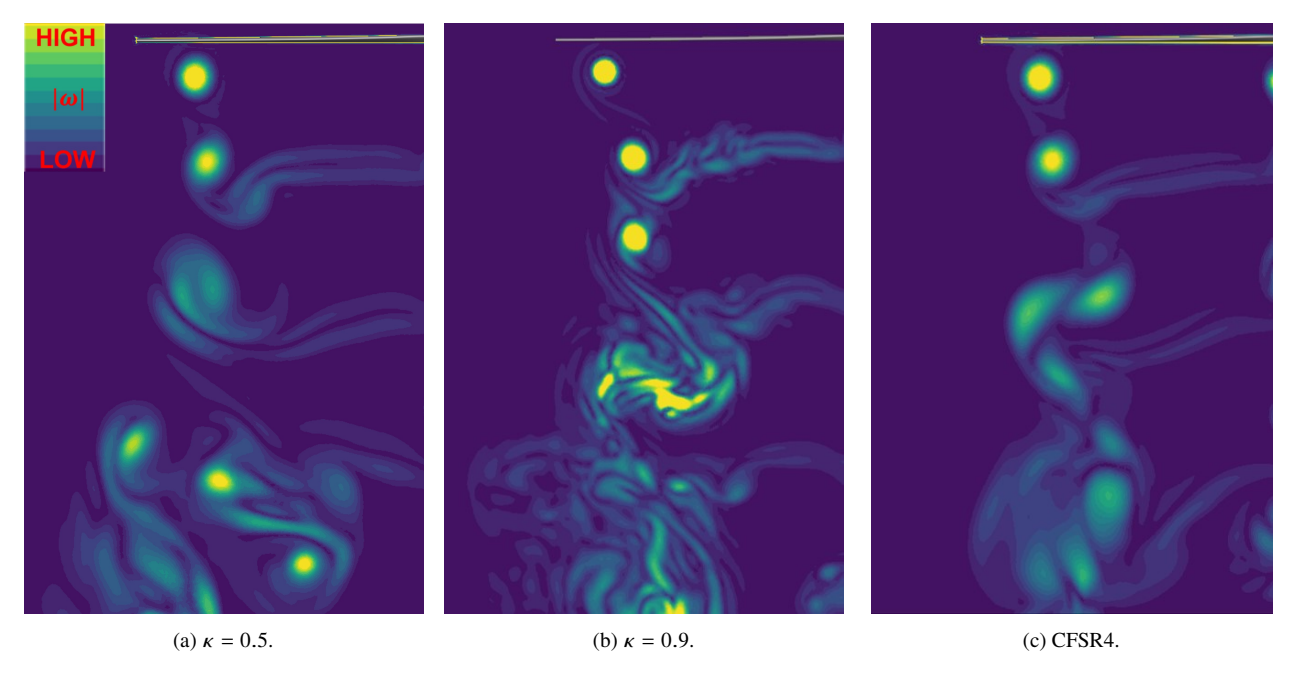


Fig. 8 OPT2 flow visualization of instantaneous vorticity magnitude along quarter-chord aligned vertical slice showing impingement of vortex from previous blade for $\Delta \psi = 0.25^{\circ}$ cases.

IV. Acoustic Results

A. Ideally Twisted Rotor

1. Tonal Noise

The first acoustic processing method described in Section II.D was used to produce a tonal noise comparison between the predictions using both temporal resolutions and measured data on an SPL narrowband basis for the ITR in Fig. 9. The observer was out-of-plane and located $\Theta_{obs} = -35^{\circ}$ below the rotor and y = 1.896 m away from the rotor or y = 11.94R. Figure 9 shows nearly identical prediction of the fundamental BPF for all ITR predictions. Since the ITR was shown in Ref. [17] to be thickness noise dominant at the fundamental BPF, it makes sense that the predictions produce similar results since the same grid system was used for these simulations. Figure 9 also shows that less numerical dissipation in the $\kappa = 0.9$ case greatly improves the tonal noise prediction at harmonics of the BPF and at shaft harmonics when compared to the $\kappa = 0.5$ case. The $\kappa = 0.9$ and CFSR4 cases predict similar tonal noise content at frequencies greater than the fundamental BPF with the $\kappa = 0.9$ case predicting the first BPF harmonic (i.e., 2*BPF) more accurately than the CFSR4 case when compared to the experiment. The CFSR4- κ case is shown to predict the second and third BPFs more accurately than the CFSR4 case in Fig. 9a. It can also be seen by comparing Figs. 9a and 9b that increasing the temporal resolution increases the prediction accuracy of the BPF harmonics, moreso for the $\kappa = 0.9$ case than for the $\kappa = 0.5$ case.

The second acoustic processing method described in Section II.D was used to establish directivity trends of the predicted fundamental BPF and second BPF for both the coarse and fine temporal resolution cases, which are compared against experimental data for the ITR in Figs. 10 and 11. Again, very similar predictions can be seen for all cases at the fundamental BPF in Fig. 10 due to the thickness noise dominance, as previously mentioned. The second BPF predicted by the $\kappa = 0.9$ case trends much better with the measured data in Fig. 11 than all other cases, with the $\kappa = 0.9$ case at $\Delta \psi = 0.125^{\circ}$ producing the best agreement with the experiment.

2. Broadband Noise

Narrowband broadband noise autospectra were produced using the third acoustic processing method described in Section II.D and are shown in Fig. 12 for the measured ITR data and the prediction cases, where the κ simulations at both temporal resolutions are displayed in Fig. 12a and the CFSR4 and CFSR4- κ cases are shown in Fig. 12b. Figure 12a

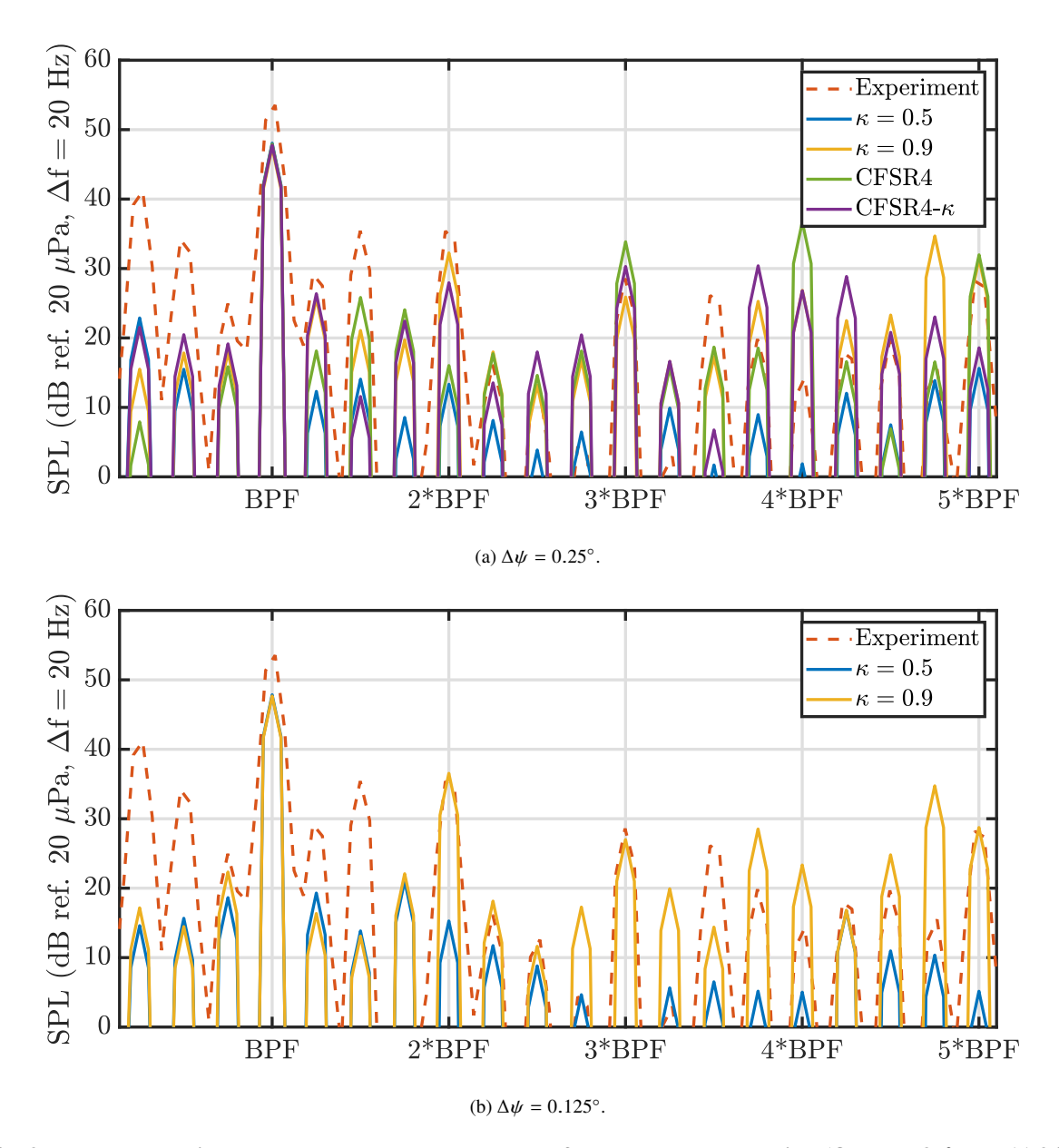


Fig. 9 ITR tonal noise narrowband spectra at the out-of-plane observer location ($\Theta_{obs}=-35^{\circ}, y=11.94R$).

shows negligible differences in the broadband noise prediction between the two temporal resolutions for the $\kappa=0.5$ case and the $\kappa=0.9$ case, respectively. These minor differences in prediction for the different temporal resolutions may signify that the grid is saturated and that no further physics can be resolved by simply refining the temporal resolution for a given inviscid numerical scheme; a spatial resolution refinement or modifications to the viscous numerical scheme may also be required to resolve finer flow features on the rotor surface and in the near wake. This figure also shows that the $\kappa=0.9$ and CFSR4 cases do a much better job at capturing some of the nondeterministic mid-frequency tones and, in general, trend better with the measured data than the $\kappa=0.5$ cases. It is also clear from Fig. 12b that decreasing dissipation in the CFSR4- κ case causes an overprediction in the broadband noise when compared to the CFSR4 case. Since the dominant broadband noise sources for the ITR at this operating condition were shown to be related to perpendicular BVIs in Ref. [12], it makes sense that spatial resolution improvements due to decreased dissipation or higher-order flux reconstruction would improve broadband noise predictions. This speculation is further fortified by the enhanced vorticity field shown in Fig. 6 for the $\kappa=0.9$ and CFSR4 cases when compared to the $\kappa=0.5$ case.

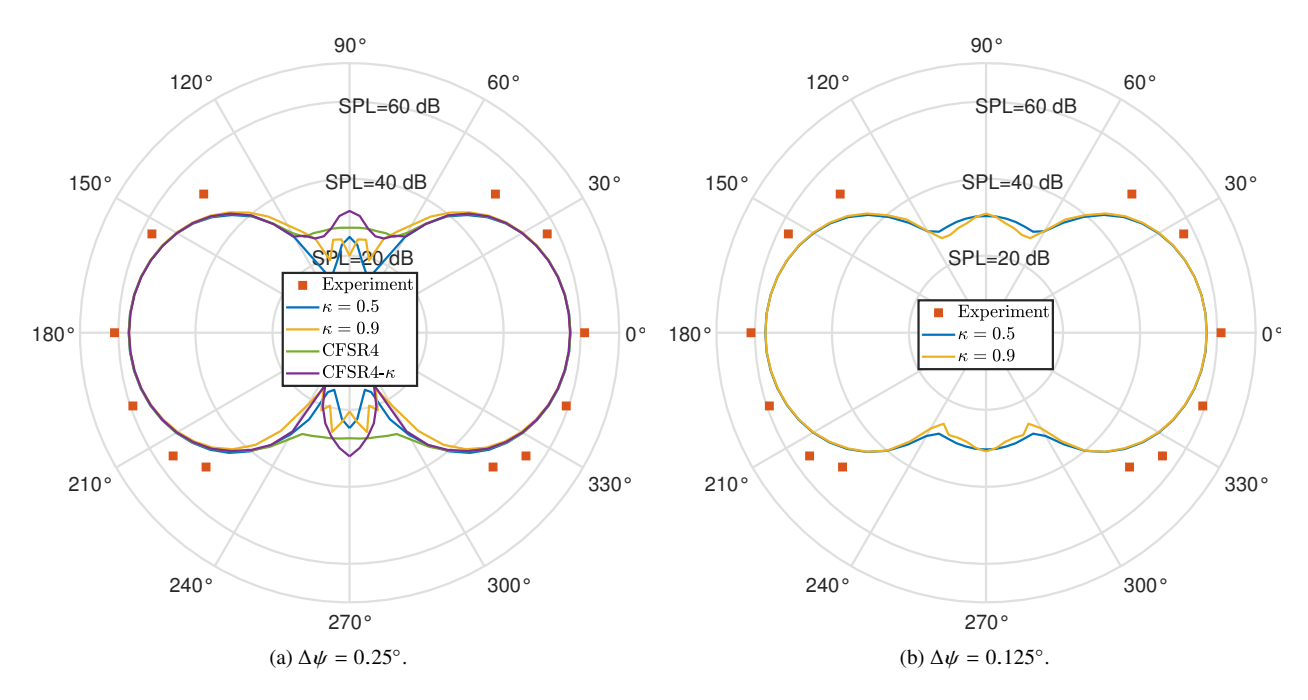


Fig. 10 ITR fundamental BPF directivity at y = 11.94R.

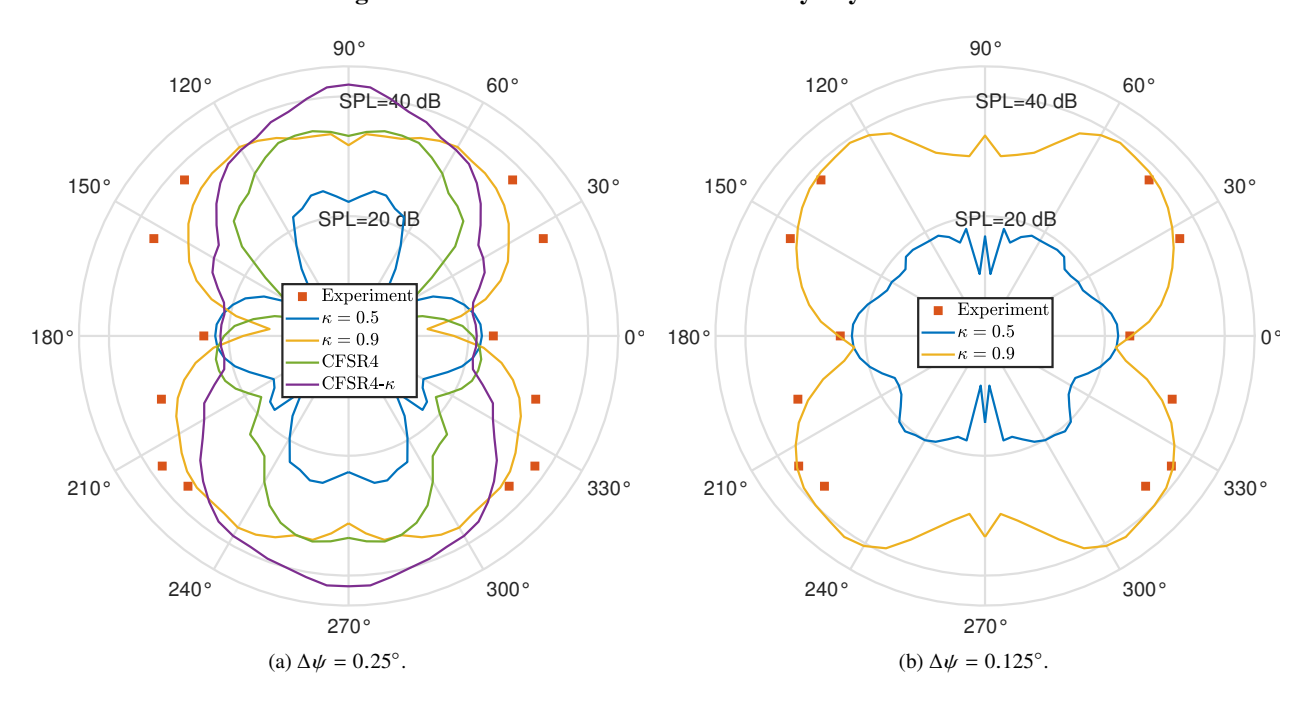
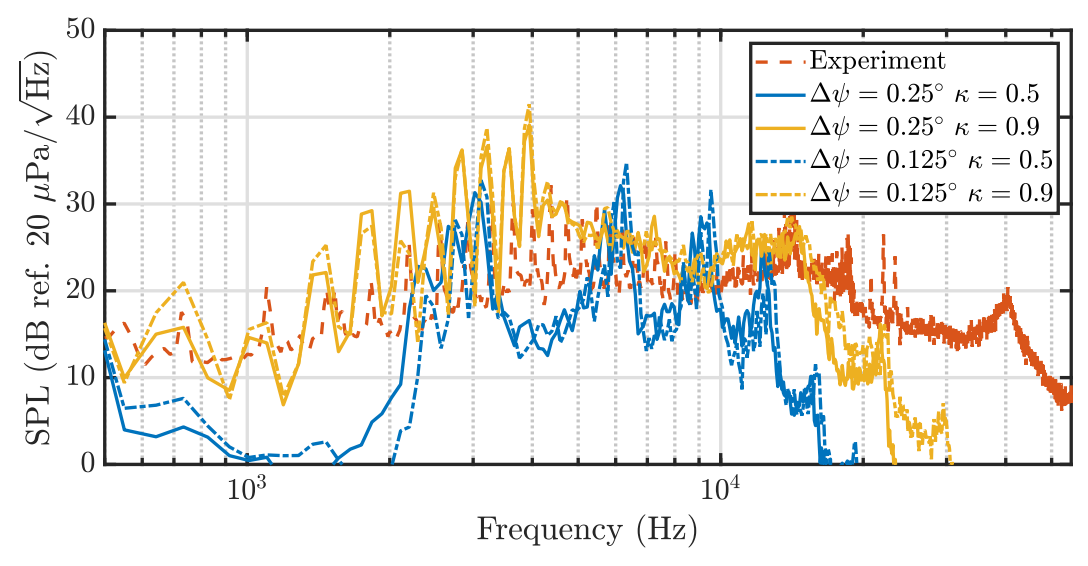


Fig. 11 ITR 2*BPF directivity at y = 11.94R.

B. Optimum Hovering 2-Bladed Rotor

1. Tonal Noise

The first acoustic processing method described in Section II.D was again used to produce a tonal noise comparison between the predictions using both temporal resolutions and measured data on an SPL narrowband basis for the OPT2 in Fig. 13. The same out-of-plane observer that was used in Fig. 9 was used; however, the nondimensional observer distance from the OPT2 rotor was y = 9.95R. The second acoustic processing method described in Section II.D was used to establish directivity trends of the predicted fundamental BPF and second BPF for all simulation cases, which are



(a) Temporal resolution comparison for $\kappa = 0.5$ and $\kappa = 0.9$ cases.

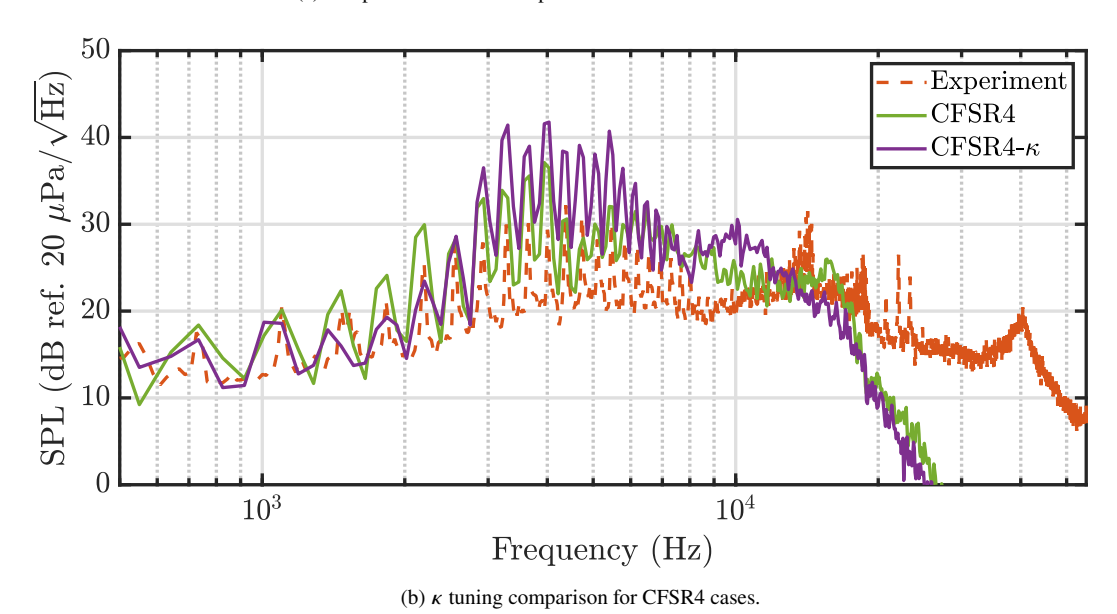


Fig. 12 ITR broadband noise narrowband autospectra at the out-of-plane observer location ($\Theta_{obs} = -35^{\circ}$, y = 11.94R).

compared against experimental data for the OPT2 in Fig. 14. Figures 13 and 14 show slightly different interpretations of the same results, and it is important to consider both when conducting analysis. First, it should be noted that the measured BPF is below the cut-on frequency of the test facility. Though Fig. 13 shows the BPF amplitude for the $\kappa = 0.9$ case at $\Delta \psi = 0.25^{\circ}$ to agree best with the measured data, the integrated quantities in Fig. 14a actually show that the other two cases (i.e., $\kappa = 0.5$ at $\Delta \psi = 0.25^{\circ}$ and $\kappa = 0.9$ at $\Delta \psi = 0.125^{\circ}$) produce better agreement with the experiment across all observer locations. It is difficult to discern experimental agreement of the second BPF in Fig. 13 due to the truncated experimental peak caused by spectral resolution. Figure 14b shows that, although the $\kappa = 0.9$ case at $\Delta \psi = 0.125^{\circ}$ agrees best with the experiment at the $\Theta_{obs} = -35^{\circ}$ observer location, the directivity pattern of the 2*BPF for this case greatly deviates from the measured data. The directivity pattern of the 2*BPF for the $\kappa = 0.9$ case at $\Delta \psi = 0.25^{\circ}$ case in Fig. 14b is shown to trend best with the measured data compared to the other two cases, though the amplitudes are underpredicted.

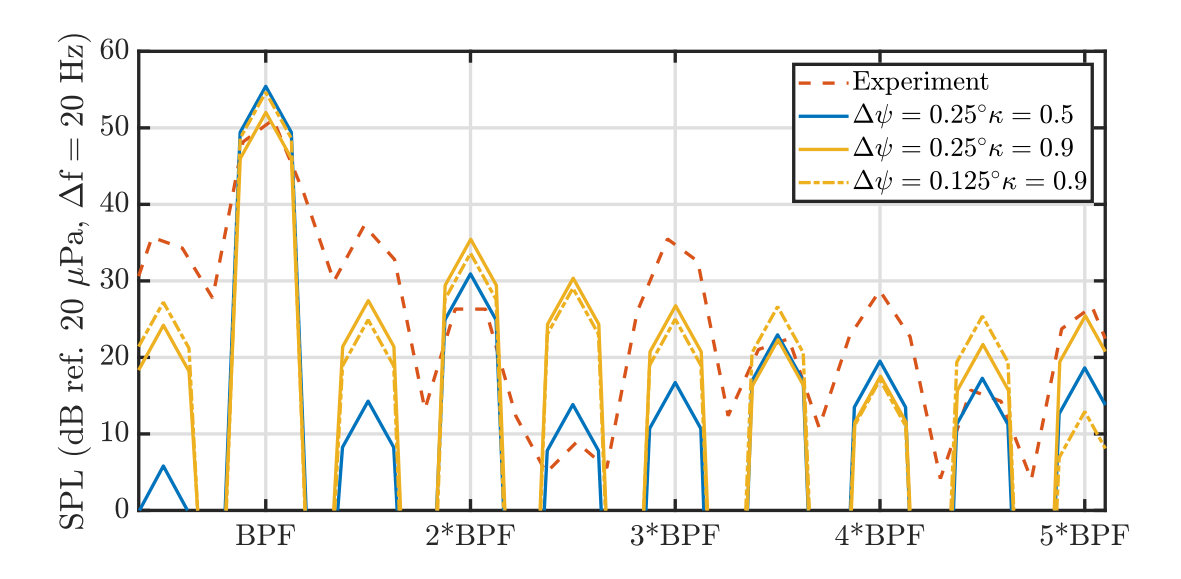


Fig. 13 OPT2 tonal noise narrowband spectra at the out-of-plane observer location ($\Theta_{obs} = -35^{\circ}$, y = 9.95R).

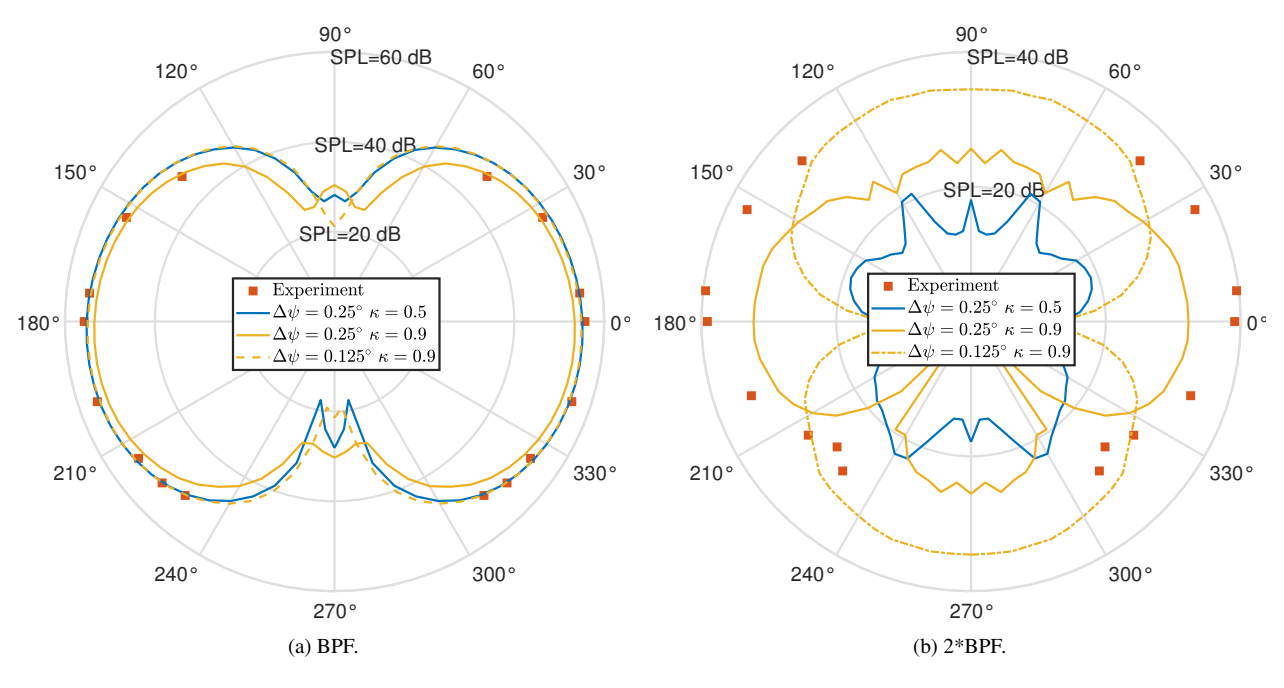


Fig. 14 OPT2 BPF directivity comparison at y = 11.94R.

2. Broadband Noise

Narrowband broadband noise autospectra were produced using the third acoustic processing method described in Section II.D and are shown in Fig. 15 for the simulation cases and measured data. A few observations can be made based on the broadband noise results shown in the figure. First, it can be seen that all three cases exhibit a spectral hump centered around approximately 7 kHz that does not appear in the measured data. Second, it can be seen that the high-frequency spectral roll-off of the $\kappa=0.9$ case at $\Delta\psi=0.125^\circ$ occurs at a higher frequency that for the other two cases, signifying that the grid is not saturated and that more flow physics were distilled by temporal resolution refinement, unlike for the ITR predictions. Furthermore, the $\kappa=0.9$ case at $\Delta\psi=0.25^\circ$ deviates less from the experiment than the other two cases at frequencies below 4 kHz. Lastly, the $\kappa=0.5$ case at $\Delta\psi=0.25^\circ$ exhibits a tone centered around approximately 8.5 kHz, which is similar in magnitude to the measured tone around 16 kHz.

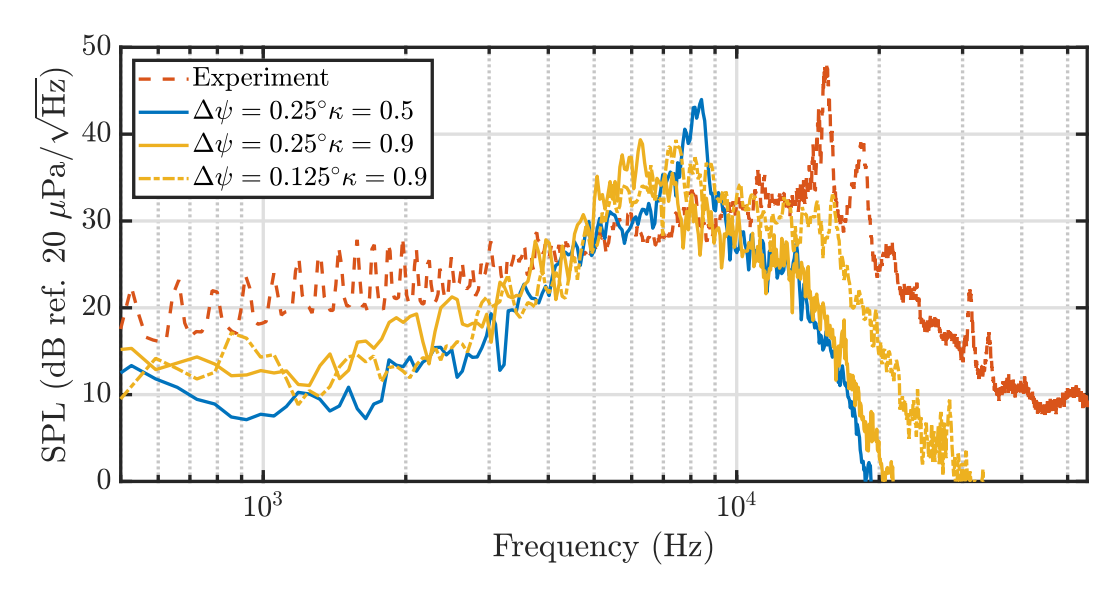


Fig. 15 OPT2 broadband noise narrowband autospectra at the out-of-plane observer location ($\Theta_{obs} = -35^{\circ}$, y = 9.95R).

V. Conclusions

A computational study was performed in this work on two sUAS rotors, the ideally twisted rotor and the optimum hovering 2-bladed rotor, using FUN3D-ANOPP2. Both of these rotors were simulated at their baseline hover operating conditions and a comparative study was performed to investigate the effects of different inviscid upwinding techniques and temporal resolutions on aerodynamic performance and acoustic prediction. Simulation results were compared against experimental measurements obtained in the Small Hover Anechoic Chamber facility at the NASA Langley Research Center.

Aerodynamic performance results showed that all simulated thrust and torque values agreed with measured data within approximately 11.0% for the ideally twisted rotor with the high-dissipation $\kappa = 0.5$ case at the high temporal resolution of $\Delta \psi = 0.125^{\circ}$ producing the best thrust agreement to the experiment (i.e., 8.02%) and the dissipation-tuned higher-order CFSR4- κ case at the low temporal resolution of $\Delta \psi = 0.25^{\circ}$ predicting the best torque agreement to the measured data (i.e., 8.92%). For the optimum hovering 2-bladed rotor, better experimental agreement was observed for the torque predictions (i.e., within 7.60%) when compared to the thrust predictions (i.e., within 18.0%) for all cases except for the CFSR4 case at the coarse temporal resolution of $\Delta \psi = 0.25^{\circ}$. The CFSR4 case at $\Delta \psi = 0.25^{\circ}$ produced the best experimental agreement in thrust (i.e., 9.69%) and the low-dissipation-tuned $\kappa = 0.9$ case at $\psi = 0.125^{\circ}$ had the best torque agreement (i.e., 3.14%). It was thought that collective pitch uncertainty and blade deflection during experimental testing could be a plausible cause for the disparate comparisons in thrust and torque prediction. Near-field aerodynamic visualizations of the vorticity field showed that differing amounts of dissipation have an affect on the turbulent field surrounding the vortex core of the first BVI, the coherence of the second and higher BVI vortex cores, and the downstream breakdown of the rotor wake. The simulation case with the most dissipation (i.e., $\kappa = 0.5$) was seen to predict the least coherent vortices and a fewer number of vortices for both rotor geometries whereas the CFSR4- κ and $\kappa = 0.9$ case predicted the most coherent vortices for the ideally twisted rotor and optimum hovering 2-bladed rotor geometries, respectively.

Acoustic prediction results showed that all cases predicted similar fundamental BPF amplitudes for the ideally twisted rotor geometry, which can be explained by the thickness noise dominance of the BPF for this rotor shown in previous works. In general, lowering the dissipation via κ tuning or by using the higher-order scheme for the ideally twisted rotor predictions produced better tonal noise agreement with the measured data and increasing the temporal resolution enhanced the tonal noise prediction for the $\kappa=0.9$ case moreso than for the $\kappa=0.5$ case. The $\kappa=0.9$ and CFSR4 cases were also seen to more accurately predict the broadband noise of the ideally twisted rotor when compared to the experiment. Negligible differences were seen in the broadband noise prediction of the ideally twisted rotor between the two temporal resolutions for both the $\kappa=0.5$ and $\kappa=0.9$ cases, signifying that the grid system may be saturated and that no additional flow physics on the geometry or in the near wake can be resolved without a

spatial resolution refinement or modifications to the viscous numerical scheme. For the optimum hovering 2-bladed rotor, accurate fundamental BPF directivity was predicted by the $\kappa=0.5$ case at $\Delta\psi=0.25^\circ$ and the $\kappa=0.9$ case at $\Delta\psi=0.125^\circ$, whereas the $\kappa=0.9$ case at $\Delta\psi=0.25^\circ$ predicted the 2*BPF directivity trend closer to the experiment than for the other cases, albeit with an amplitude underprediction. For the broadband noise prediction of the optimum hovering 2-bladed rotor, the high-frequency spectral roll-off was seen to occur at a higher frequency when increasing the temporal resolution of the $\kappa=0.9$ case. The broadband noise predictions also exhibited different spectral shapes when compared to the experiment for the optimum hovering 2-bladed rotor. For this rotor geometry, the $\kappa=0.5$ case at $\Delta\psi=0.25$ predicted a tone around 8.5 kHz, which was similar in amplitude to the experimental tone centered around 16 kHz.

VI. Acknowledgments

The authors would like to thank Nikolas Zawodny and Nicole Pettingill from the Aeroacoustics Branch at the NASA Langley Research Center for providing the experimental data used for comparison in this work. This work was funded by the NASA Revolutionary Vertical Lift Technology (RVLT) project. Computational resources supporting this work were provided by the Midrange HPC K-Cluster at the NASA Langley Research Center and by the NASA High-End Computing (HEC) Program through the NASA Advanced Supercomputing (NAS) Division at the NASA Ames Research Center.

References

- [1] Zawodny, N. S., Boyd Jr., D. D., and Burley, C. L., "Acoustic Characterization and Prediction of Representative, Small-Scale Rotary-Wing Unmanned Aircraft System Components," *AHS International 72nd Annual Forum & Technology Display*, West Palm Beach, FL, May 2016.
- [2] Greenwood, E., Brentner, K. S., Rau, R. F., and Gan, Z. F. T., "Challenges and Opportunities for Low Noise Electric Aircraft," *International Journal of Aeroacoustics*, Vol. 21, No. 5–7, 2022, pp. 315–381.
- [3] Thurman, C. S., Zawodny, N. S., Pettingill, N. A., Lopes, L. V., and Baeder, J. D., "Physics-informed Broadband Noise Source Identification and Prediction of an Ideally Twisted Rotor," AIAA SciTech 2021 Forum, AIAA Paper 2021–1925, Virtual, January 2021.
- [4] Thurman, C. S., Zawodny, N. S., and Baeder, J. D., "Computational Prediction of Broadband Noise from a Representative Small Unmanned Aerial System Rotor," *VFS International 76th Annual Forum & Technology Display*, Virtual, October 2020.
- [5] Li, S., and Lee, S., "UCD-QuietFly: A New Program to Predict Multi-Rotor eVTOL Broadband Noise," 2020 VFS Aeromechanics for Advanced Vertical Flight Technical Meeting, San Jose, CA, January 2020.
- [6] Ffowcs Williams, J. E., and Hawkings, D. L., "Sound Generation by Turbulence and Surfaces in Arbitrary Motion," *Philosophical Transactions of the Royal Society of London. Series A, Mathematical and Physical Sciences*, Vol. 264, No. 1151, 1969, pp. 321–342.
- [7] Thurman, C. S., "Computational Study of Boundary Layer Effects on Stochastic Rotor Blade Vortex Shedding Noise," *Aerospace Science and Technology*, Vol. 131A, No. 107983, 2022.
- [8] Casalino, D., Romani, G., Zhang, R., and Chen, H., "Lattice-Boltzmann Calculations of Rotor Aeroacoustics in Transitional Boundary Layer Regime," *Aerospace Science and Technology*, Vol. 130, No. 107953, 2022.
- [9] Casalino, D., Romani, G., Maria Pii, L., and Colombo, R., "Sensitivity of Laminar Separation Noise from a Rotor to Inflow Turbulence," *AIAA AVIATION 2023 Forum*, AIAA Paper 2023–3220, San Diego, CA, June 2023.
- [10] Kunz, F. T., Pullin, S., Zhou, B. Y., Azarpeyvand, M., Galimberti, L., Morelli, M., and Guardone, A., "High-Fidelity Propeller Broadband Noise Prediction using SU2," AIAA AVIATION 2023 Forum, AIAA Paper 2023–4185, San Diego, CA, June 2023.
- [11] Rendón, J., Moreau, S., Gojon, R., and Bauerheim, M., "LBM and iLES Comparison for the Aerodynamic and Acoustic Characteristics of a Low-Speed Rotor," 30th AIAA/CEAS Aeroacoustics Conference, AIAA Paper 2024–3046, Rome, Italy, June 2024.
- [12] Thurman, C. S., Boyd Jr., D. D., and Lopes, L. V., "Prediction of Broadband Blade-Wake Back-Scatter Noise from a Hovering Ideally Twisted Rotor using OVERFLOW2-ANOPP2," AIAA SciTech 2024 Forum, AIAA Paper 2024–2471, Orlando, FL, January 2024.

- [13] Thurman, C. S., Boyd Jr., D. D., Buning, P. G., Reboul, G., and Benoit, C., "NASA/ONERA Collaboration on Small Hovering Rotor Broadband Noise Prediction using Lattice-Boltzmann Method and Structured Navier-Stokes Solvers," 30th AIAA/CEAS Aeroacoustics Conference, AIAA Paper 2024–3106, Rome, Italy, June 2024.
- [14] Mankbadi, R. R., Afari, S. O., and Golubev, V. V., "High-Fidelity Simulations of Noise Generation in a Propeller-Driven Unmanned Aerial Vehicle," *AIAA Journal*, Vol. 59, No. 3, 2021, pp. 1020–1039.
- [15] Broatch, A., Navarro, R., García-Tíscar, J., and Ramírez, F. N., "Evaluation of Different FW-H Surfaces and Modal Decomposition Techniques for the Acoustic Analysis of UAV Propellers through Detached Eddy Simulations," *Aerospace Science and Technology*, Vol. 146, No. 108956, 2024.
- [16] Thurman, C. S., Zawodny, N. S., and Pettingill, N. A., "The Effect of Boundary Layer Character on Stochastic Rotor Blade Vortex Shedding Noise," VFS International 78th Annual Forum & Technology Display, Fort Worth, TX, May 2022.
- [17] Pettingill, N. A., Zawodny, N. S., Thurman, C. S., and Lopes, L. V., "Acoustic and Performance Characteristics of an Ideally Twisted Rotor in Hover," *AIAA SciTech 2021 Forum*, AIAA Paper 2021–1928, Virtual, January 2021.
- [18] Chaderjian, N. M., "Quantitative Approach for the Accurate CFD Simulaton of Hover in Turbulent Flow," *Eleventh International Conference on Computational Fluid Dynamics*, Maui, HI, July 2022.
- [19] Anderson, W. K., Biedron, R. T., Carlson, J.-R., Derlaga, J. M., Diskin, B., Druyor Jr., C. T., Gnoffo, P. A., Hammond, D. P., Jacobson, K. E., Jones, W. T., Kleb, B., Lee-Rausch, E. M., Liu, Y., Nastac, G. C., Nielsen, E. J., Padway, E. M., Park, M. A., Rumsey, C. L., Thomas, J. L., Thompson, K. B., Walden, A. C., Wang, L., Wood, S. L., Wood, W. A., and Zhang, X., "FUN3D Manual: 14.0.2," NASA TM 20230004211, https://fun3d.larc.nasa.gov/papers/FUN3D_INTG_Manual-14.0.2.pdf, 2023.
- [20] Wang, L., Anderson, W. K., Nielsen, E. J., Balakumar, P., Park, M. A., Carlson, J.-R., Iyer, P. S., and Diskin, B., "Wall-Modeled Large-Eddy Simulations for High-Lift Configurations using FUN3D," AIAA SciTech 2022 Forum, AIAA Paper 2022–1555, San Diego, CA, January 2022.
- [21] Wang, L., Anderson, W. K., Nielsen, E. J., Iyer, P. S., and Diskin, B., "Wall-Modeled Large-Eddy Simulation Method for Unstructured-Grid Navier-Stokes Solvers," AIAA SciTech 2023 Forum, AIAA Paper 2023–0251, National Harbor, MD, January 2023.
- [22] Balakumar, P., Iyer, P. S., Nielsen, E. J., Anderson, W. K., Wang, L., and Diskin, B., "Assessment of UMUSCL Scheme for DNS of Turbulent Flows," AIAA SciTech 2024 Forum, AIAA Paper 2024–2199, Orlando, FL, January 2024.
- [23] Vatsa, V. N., and Lockard, D. P., "Assessment of Hybrid RANS/LES Turbulence Models for Aeroacoustics Applications," *16th AIAA/CEAS Aeroacoustics Conference*, AIAA Paper 2010–4001, Stockholm, Sweden, June 2010.
- [24] Vatsa, V. N., Lockard, D. P., and Khorrami, M. R., "Application of FUN3D Solver for Aeroacoustics Simulation of a Nose Landing Gear Configuration," *17th AIAA/CEAS Aeroacoustics Conference*, AIAA Paper 2011–2820, Portland, OR, June 2011.
- [25] Biedron, R. T., and Lee-Rausch, E. M., "Rotor Airloads Prediction using Unstructured Meshes and Loose CFD/CSD Coupling," 26th AIAA Applied Aerodynamics Conference, AIAA Paper 2008–7341, Honolulu, HI, August 2008.
- [26] Wang, L., Diskin, B., Biedron, R. T., Nielsen, E. J., and Bauchau, O. A., "High-Fidelity Multidisciplinary Sensitivity Analysis and Design Optimization for Rotorcraft Applications," *AIAA Journal*, Vol. 57, No. 8, 2019, pp. 3117–3131.
- [27] Wang, L., Diskin, B., Lopes, L. V., Nielsen, E. J., Lee-Rausch, E. M., and Biedron, R. T., "High-Fidelity Aeroacoustic Optimization Tool for Flexible Rotors," *Journal of the American Helicopter Society*, Vol. 66, No. 2, 2021, pp. 1–16.
- [28] Liu, Y., and Wang, L., "High-Fidelity Simulations of Lift+Cruise VTOL Urban Air Mobility Concept Aircraft in Hover," AIAA SciTech 2024 Forum, AIAA Paper 2024–1118, Orlando, FL, January 2024.
- [29] Roe, P. L., "Approximate Riemann Solvers, Parameter Vectors, and Difference Schemes," *Journal of Computational Physics*, Vol. 43, No. 2, 1981, pp. 357–372.
- [30] Burg, C. O. E., "Higher Order Variable Extrapolation for Unstructured Finite Volume RANS Flow Solvers," 17th AIAA Computational Fluid Dynamics Conference, AIAA Paper 2005–4999, Toronto, Ontario, Canada, June 2005.
- [31] Yang, H. Q., and Harris, R. E., "Development of Vertex-Centered High-Order Schemes and Implementation in FUN3D," *AIAA Journal*, Vol. 54, No. 12, 2016, pp. 3742–3760.

- [32] Padway, E. M., and Nishikawa, H., "High-Order/Low-Dissipation Chain-Rule Flux Solution Reconstruction Schemes in FUN3D," *AIAA SciTech 2024 Forum*, AIAA Paper 2024–1749, Orlando, FL, January 2024.
- [33] Nishikawa, H., "Economically High-Order Unstructured-Grid Methods: Clarification and Efficient FSR Schemes," *International Journal for Numerical Methods in Fluids*, Vol. 93, No. 11, 2021, pp. 3187–3214.
- [34] Vatsa, V. N., Carpenter, M. H., and Lockard, D. P., "Re-evaluation of an Optimized Second Order Backward Difference (BDF2OPT) Scheme for Unsteady Flow Applications," 48th AIAA Aerospace Sciences Meeting Including the New Horizons Forum and Aerospace Exposition, AIAA Paper 2010–0122, Orlando, FL, January 2010.
- [35] Spalart, P. R., Deck, S., Shur, M. L., Squires, K. D., Strelets, M. K., and Travin, A., "A New Version of Detached-eddy Simulation, Resistant to Ambiguous Grid Densities," *Theoretical and Computational Fluid Dynamics*, Vol. 20, 2006, pp. 181–195.
- [36] Lopes, L., and Burley, C., "ANOPP2 User's Manual: Version 1.2," NASA TM 2016-219342, 2016.
- [37] Farassat, F., and Succi, G. P., "The Prediction of Helicopter Discrete Frequency Noise," *Vertica*, Vol. 7, No. 4, 1983, pp. 309–320.
- [38] Brentner, K., and Farassat, F., "Modeling Aerodynamically Generated Sound of Helicopter Rotors," *Progress in Aerospace Sciences*, Vol. 39, No. 2–3, 2003, pp. 83–120.
- [39] Lopes, L., "ANOPP2's Farassat Formulations Internal Functional Modules (AFFIFMs) Reference Manual," NASA TM 20210021111, 2021.
- [40] Thurman, C. S., "Preliminary Solver Comparison for Aeroacoustic Prediction of a Small Hovering Rotor," *NASA Acoustics Technical Working Group Meeting*, Hampton, VA, March 2024.